Materials Research. 2017; 20(6): 1669-1680
DOI: http://dx.doi.org/10.1590/1980-5373-MR-2017-0204

Electrochemical Study of the AISI 409 Ferritic Stainless Steel: Passive Film Stability and Pitting Nucleation and Growth

Juliana Sarango de Souza[a], Leandro Antônio de Oliveira[b], Isaac Jamil Sayeg[c], Renato Altobelli Antunes[b]*

[a]Departamento de Ciências Exatas e da Terra, Universidade Federal de São Paulo (UNIFESP), 09910-720, Diadema, SP, Brasil.
[b]Centro de Engenharia, Modelagem e Ciências Sociais Aplicadas (CECS), Universidade Federal do ABC (UFABC), 09210-580, Santo André, SP, Brasil.
[c]Instituto de Geociências, Universidade de São Paulo, Rua do Lago, 562, 05508-080, São Paulo, SP, Brasil.

Received: February 19, 2017; Revised: August 09, 2017; Accepted: August 21, 2017

The aim of the present work was to study the passive film stability and pitting corrosion behavior of the AISI 409 stainless steel. The electrochemical tests were carried out in 0.1 M NaCl solution at room temperature. The general electrochemical behavior was assessed using electrochemical impedance spectroscopy (EIS) measurements whereas the semiconducting properties of the passive film were evaluated by the Mott-Schottky approach. Pitting corrosion was investigated using potentiodynamic and potentiostatic polarization tests. Surface morphology was examined using confocal laser scanning microscopy and scanning electron microscopy (SEM). Energy dispersive X-ray spectroscopy (EDS) analyses were carried out to identify the composition of precipitates that could act as preferential sites for the onset of pitting corrosion. The results showed that the passive film presents n-type semiconductive behavior. Grain boundaries played an important role as pitting initiation sites for the AISI 409 stainless steel.

Keywords: *stainless steel, pitting corrosion, passive film stability, AISI 409.*

1. Introduction

AISI 409 is a ferritic stainless steel commonly used in automotive exhaust systems as well as farm equipment, structural supports and transformers[1]. A new trend for the ferritic stainless steels market is related to civil engineering applications such as the transport of drinking water[2,3]. The engineering applications of the AISI 409 stainless steel have been established due to its relatively low cost and good corrosion resistance at high temperatures. This material is a titanium-stabilized grade with low carbon content[4]. The presence of titanium and the low carbon content are typical features for decreasing the susceptibility to intergranular corrosion during welding operations or high temperature applications such as for components of automotive exhaust systems. Titanium has greater affinity for carbon than chromium, preferentially forming precipitates with this element instead of chromium carbide precipitates. Thus, the traditional sensitization mechanism of stainless steels by the precipitation of chromium-rich carbides would be prevented[5,6]. However, titanium-rich precipitation can lead to the formation of galvanic couples in the microstructure of ASI 409 stainless steels due to the different activity between the ferrite matrix and the precipitates. In this respect, localized corrosion attack would be triggered by the presence of titanium-rich precipitates[6]. TiC, Ti(C,N) and TiN precipitates have been reported to play a role in the onset of pitting corrosion of the AISI 409 stainless steel[7].

In spite of the critical role of pitting corrosion to the safe operation of stainless steel components[8-10], few studies were devoted to investigate this phenomenon on the AISI 409 grade. Balusamy et al.[11] studied the effect of grain size and microstrain induced by surface nanocrystallization after surface mechanical attrition treatment (SMAT) for different times and using different ball sizes on the corrosion behavior of AISI 409 stainless steel samples. They observed that the corrosion behavior depends on the ability of SMAT to promote passivity. When the treatment conditions (ball size and treatment time) enabled the formation of a stable passive film, corrosion resistance was increased with respect to the untreated surface due to nanocrystallization. However, for more aggressive conditions (especially for high ball sizes) corrosion was facilitated due to an increase in defect density. Ha et al.[12] evaluated the effect of non-metallic inclusions on the pitting corrosion behavior of 409L stainless steels refined by the argon oxygen decarburization (AOD) and vacuum oxygen decarburization (VOD) processes. They observed localized corrosion around oxides (Ti, Ca) suggesting that

*e-mail: renato.antunes@ufabc.edu.br

these inclusions may act as active sites for pit nucleation for samples refined by the AOD process. Titanium nitrides were found in samples prepared by the VOD process and they appeared to be immune to localized corrosion in 0.5 M NaCl at 25 ºC. Other authors studied that welding operations decreased the pitting corrosion resistance of the AISI 409 stainless steel but the investigation was focused on intergranular corrosion rather than on the pitting corrosion mechanism. Notwithstanding, the presence of titanium-rich precipitates was confirmed and the onset of localized attack was affected by the type of precipitates formed during heating and subsequent cooling from the welding temperature[13].

Although the reports mentioned above bring useful information regarding the pitting corrosion behavior of the AISI 409 stainless steel, a systematic approach correlating microstructural features with the stability of the passive film, localized corrosion mechanism and pitting morphology of this material is not found in the literature. The aim of the present work was to fill this gap by investigating the passive film resistance and pitting corrosion behavior of AISI 409 stainless steel specimens using potentisotatic and potentiodynamic polarization tests, electrochemical impedance spectroscopy measurements and evaluating the semiconducting properties of the passive film by the Mott-Schottky approach. The microstructure of the alloy was studied using scanning electron microscopy (SEM) coupled with energy dispersive X-ray spectroscopy (EDS).

2. Experimental procedure

2.1 Material and sample preparation

The material used in this work was a 2.0 mm thick cold-rolled AISI 409 ferritic stainless steel sheet. The steel was tested in the as-received condition. Its nominal chemical composition is shown in Table 1.

The steel sheet was cut into pieces of approximately 1.0 cm^2 for the EIS, Mott-Schottky and potentiodynamic tests. For potentiostatic tests small-sized specimens were prepared with an area of approximately 0.1 cm^2. This procedure was employed to prevent overlap of current transients. Next, the working electrodes were prepared by connecting the stainless steel pieces to a copper wire by means of a colloidal liquid conductive silver paste. The non-working surface areas were sealed with nail polish to prevent crevice corrosion. Next, the specimens were embedded in cold-curing epoxy resin. The exposed surface of each electrode was finished by wet-grinding with a series of emery papers from 200 to 2500 grit. Lastly, the working electrodes were polished with diamond past with 6 μm.

2.2 Electrochemical tests

All electrochemical tests were carried out using a potentiostat/galvanostat Autolab M101. The experimental set-up consisted of a conventional three-electrode cell with a platinum wire as the counter-electrode, Ag/AgCl as reference and the AISI 409 samples as working electrodes. The tests were performed in 0.1 M NaCl solution at room temperature.

Three different sets of experiments were performed. The first one is comprised of an evaluation of the general electrochemical response of the electrode surface using electrochemical impedance spectroscopy (EIS) followed by analysis of the semiconducting properties of the passive film by the Mott-Schottky approach. Initially, the open circuit potential was monitored for 24 h in order to ensure a steady state condition. Next, EIS measurements were performed at the open circuit potential (OCP) in the frequency range from 100 kHz to 10 mHz with an amplitude of the perturbation signal of ±10 mV (rms) and an acquisition rate of 10 points per decade. Right after the EIS measurements, Mott-Schottky plots were acquired at a fixed frequency of 1 kHz. The potential was scanned from +0.3 $V_{Ag/AgCl}$ versus the OCP back to the OCP in the cathodic direction with a step of 25 mV. The results were used to characterize the passive film on the surface of the AISI 409 stainless steel electrodes.

The pitting corrosion behavior was characterized by potentiodynamic and potentiostatic polarization tests. Thus, a second set of experiments was comprised of an initial monitoring of the OCP for 24 h. Next, the samples were potentiodynamically polarized from the open circuit potential up to +1.0 $V_{Ag/AgCl}$. The sweep rate was 1 $mV.s^{-1}$.

Another set of specimens was potentiostatically polarized at the anodic potentials of +100 mV and +200 mV with respect to the OCP for 1800 s. The OCP was initially monitored for 24 h before potentiostatic polarization. This procedure was employed to detect metastable pitting. All the electrochemical tests were conducted in triplicate.

2.3 Microstructural characterization and pit morphology

The microstructure of the AISI 409 stainless steel was observed using optical microscopy (Zeiss Axio Cam ICc 5) and scanning electron microscopy (Leica/Leo 440 I and Jeol/JSM-6010). Elemental composition of precipitates within the ferrite matrix was determined using energy dispersive X-ray spectroscopy (EDS) analysis. Pit morphology was

Table 1. Nominal chemical composition of the AISI 409 stainless steel.

Composition (wt.%)									
C	Mn	Si	Cr	Ni	P	S	N	Ti	Fe
0.03 max	1.00 max	1.00 max	10.5 – 11.7 max	0.50 max	0.04 max	0.02 max	0.03 max	8x(C+N) min	Bal.

examined using confocal laser scanning microscopy (CLSM) (LEXT OLS4100 Olympus). X-ray diffraction (XRD) was used to confirm the ferritic structure of the samples and to check for the presence of any additional phases. The analysis was carried out in a Rigaku Multiflex diffractometer in the Bragg-Brentano θ-2θ geometry, using Cu-kα radiation. The angular range was scanned from 35º to 120º in 2θ with a step size of 0.5º and 25 s of acquisition time per step.

3. Results and Discussion

3.1 Microstructural Characterization

Figure 1a shows an optical micrograph of the AISI 409 stainless steel used in the present work. The sample was etched in a aqueous solution containing $FeCl_3$ and HCl. The ferrite grains are clearly visible. The ferritic structure was confirmed by XRD as shown in Fig. 1b. Only Fe-α peaks were observed (JCPDS 6-0696). Notwithstanding, the presence of precipitates was detected, as suggested by the optical micrograph of a non-etched sample shown in Fig. 1c. Titanium-rich precipitates have been identified in Ti-stabilized ferritic stainless steels. The presence of TiN, TiC and Ti(C,N) has been reported[7,14,15]. In this respect, the microstructure of the AISI 409 stainless steel was further characterized by SEM/EDS analysis in order to identify the precipitates observed in Figs. 1(a) and 1(c).

SEM micrographs in the backscattered electrons (BSE) mode of the AISI 409 stainless steel are shown in Fig. 2. Imaging in the SEM-BSE mode allows distinguishing between microstructural features with atomic number contrast[16], thus ensuing the identification of small precipitates within a metallic matrix.

The general aspect of the sample can be observed in Fig. 2a. Several small and dark features can be observed within the grey ferrite matrix. A more detailed view of the surface is presented in Fig. 2b. The elemental compositions of four selected precipitates were determined using the EDS

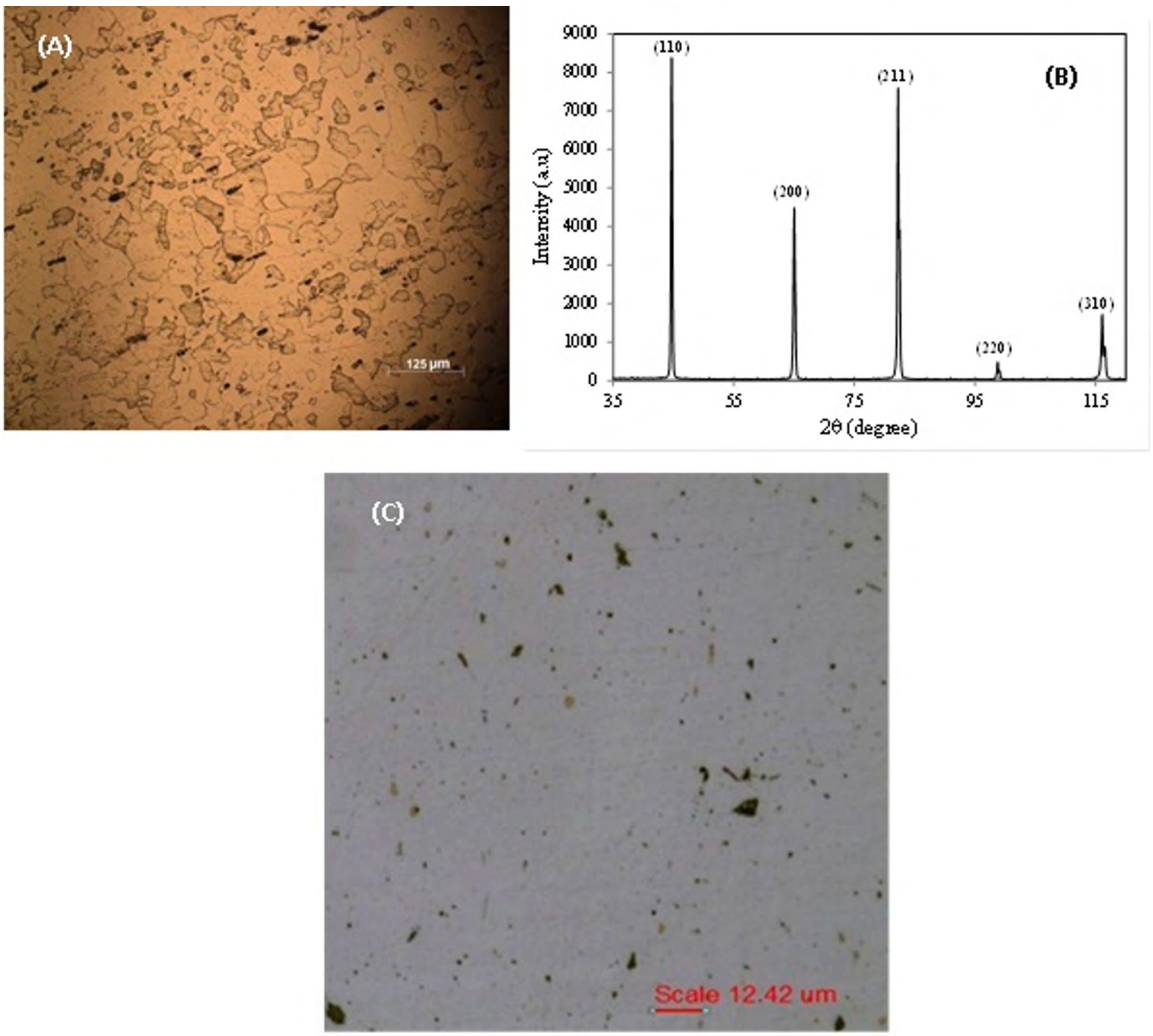

Figure 1. Microstructure and crystalline phases of the AISI 409 stainless steel samples: (a) Optical micrograph: etched sample; (b) XRD pattern; (c) optical micrograph: non etched sample.

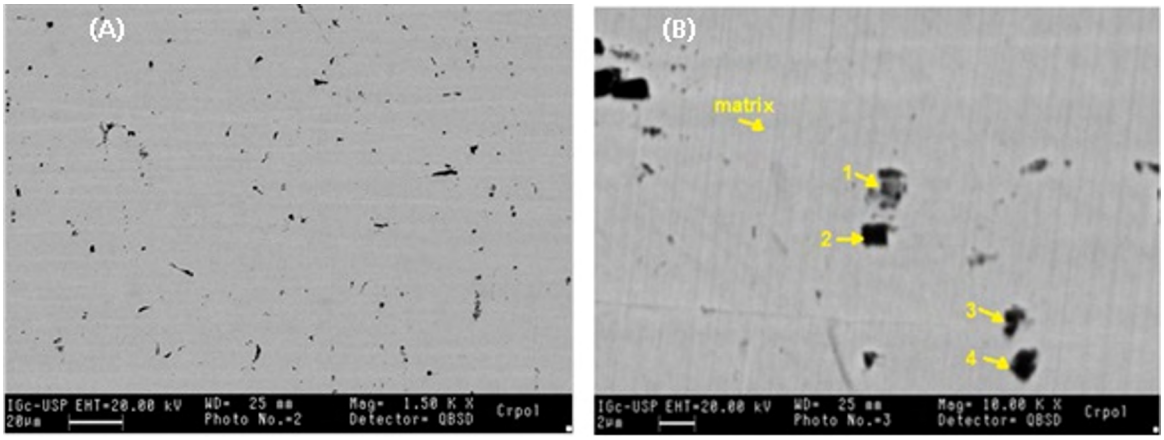

Figure 2. SEM micrographs of the AISI 409 stainless steel: a) General view; b) Detailed view showing precipitates with different morphologies.

detector coupled to the SEM instrument. These precipitates are numbered in Fig. 2b. The ferrite matrix is indicated as well. The EDS spectra of these regions are shown in Fig. 3.

The spectrum referred to the ferrite matrix is mainly characterized by the main peaks of iron and chromium, as expected. Titanium peaks were observed for the precipitates 1, 2, 3 and 4. The main difference between the precipitates can be ascribed to the presence of carbon and nitrogen. While nitrogen was identified in precipitates 1 and 2 it was absent in the precipitates 3 and 4. According to Michelic et al.[7] the morphology is important to confirm the composition of precipitates in titanium-stabilized ferritic stainless steel. In this respect, rectangular precipitates are associated with pure TiN whereas, nitrogen-containing Ti-rich precipitates with irregular morphology are associated with Ti(C,N) precipitates. The absence of nitrogen in precipitates 3 and 4 suggest that they consist of TiC. Very small TiC can also be present in titanium-stabilized ferritic stainless steels as indicated by Kim et al.[15]. Thus, titanium-rich precipitates were unequivocally identified by SEM/EDS analysis. The corrosion behavior of ferritic stainless steels can be affected by these precipitates as confirmed by the intergranular corrosion studies published by Kim et al.[15]. In the next sections, we investigate the pitting corrosion behavior of the AISI 409 stainless steel and its relationship with the microstrucutural features described in the present section.

3.2 Electrochemical tests

3.2.1 EIS measurements

EIS measurements were performed to characterize the general corrosion behavior of the AISI 409 stainless steel with respect to the stability of the oxide film in the electrolyte. The tests were performed in a 0.1 M NaCl solution at room temperature after an initial 24 h-period of OCP monitoring. The variation of the OCP with time is shown in Fig. 4. After an initial instability period, the OCP continuously decreased up to 67 ks of immersion. Then, a steady-state condition was reached up to the end of the test.

The EIS plots are shown in Fig. 5. The Nyquist plot is characterized by a capacitive loop that is little flattened in the low frequency domain (Fig. 5a). This behavior is typical of passive metals such as stainless steels[17,18]. Bode plots are shown in Fig. 5b (phase angle and impedance modulus). The Bode phase angle plot presents a wide plateau extending from 10^2 to 10^0 Hz with the maximum phase angle reaching approximately -80º. A pure capacitive behavior is associated with a phase angle of -90º[19], indicating an electrode interface that is capable of accumulating electrical charges, avoiding migration of aggressive species such as O^{2-} and Cl^- from the solution across the interface[20]. The closer the phase angle is to -90º, the more perfect is the capacitive response of the electrode surface[21]. Hence, the AISI 409 stainless steel studied in the present work presented an EIS response close to that of a perfect capacitive behavior, suggesting it presents high corrosion resistance[22]. Furthermore, the impedance modulus at low frequencies is high and the plot is characterized by a slope of -1 which is typically observed for capacitive surfaces[23]. The phase angles slightly decreased below 10^0 Hz, indicating high surface stability with respect to the onset of charge transfer reactions and loss of corrosion resistance[24].

Electrical equivalent circuits (EECs) are often used to simulate the experimental EIS data, giving a physical interpretation for the electrochemical response of the different interfaces of the electrode in the electrolyte[25,26]. The data were modeled using a one-time constant EEC (Fig. 6). This EEC was adopted to describe the interface between electrolyte and surface oxides of uncoated stainless steels[27-29]. The fitted data are shown along with the experimental data in Fig. 5. In this model, constant phase elements (CPEs) are considered instead of pure capacitors to account for the heterogeneities of the electrode surface[30]. The impedance of a CPE (Z_{CPE}) is defined in equation (1) where $j^2 = -1$ is the imaginary number, ω is the angular frequency, Q is the

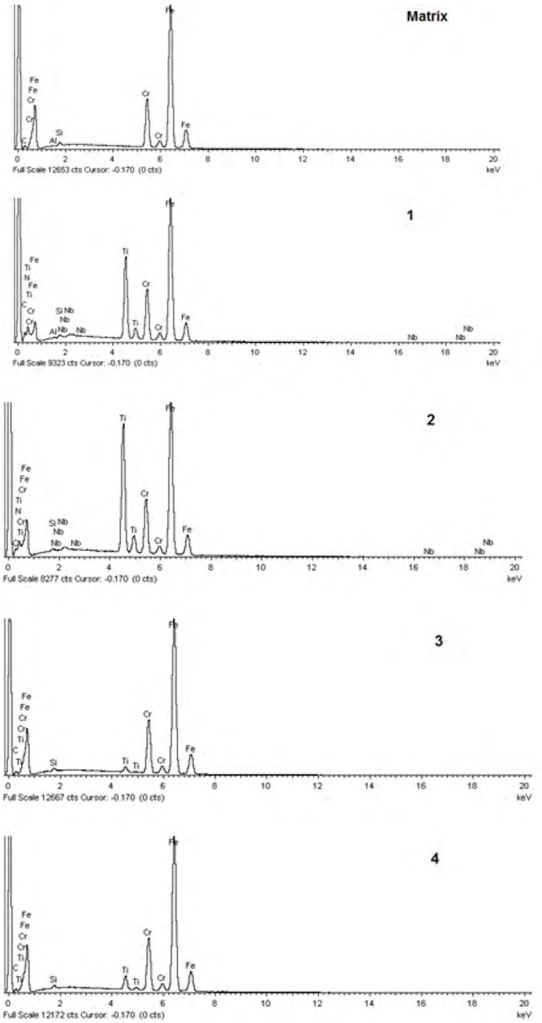

Figure 3. EDS spectra of matrix and precipitates of the AISI 409 stainless steel sample. The spectra are referred to the regions identified in Fig. 2b.

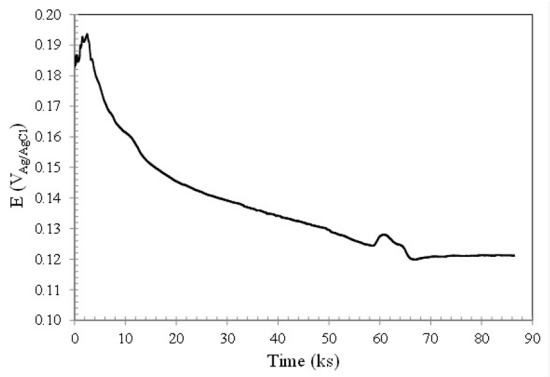

Figure 4. Open circuit potential versus time curve for the AISI 409 stainless steel in 0.1 M NaCl solution at room temperature.

magnitude of the CPE (related to its capacitance) and n is the exponent of the CPE is related to the roughness of the surface[31]. The value of n denotes the deviation from the

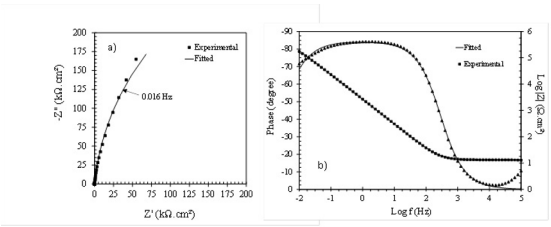

Figure 5. EIS results for the AISI 409 stainless steel after immersion for 24 h in 0.1 M NaCl solution at room temperature: a) Nyquist, b) Bode plots.

pure capacitive behavior. For an ideal capacitor n = 1, for diffusion-controlled processes n = 0.5 [32].

$$Z_{CPE} = \left[Q(j\omega)^n\right]^{-1} \quad (1)$$

The physical meaning of each element is described as follows: R_1 is the electrolyte resistance, Q_1 and R_2 are the double layer capacitance and charge transfer resistance, respectively. The values of the circuit parameters are displayed in Table 2. Good fitting quality was achieved as shown in Fig. 5.

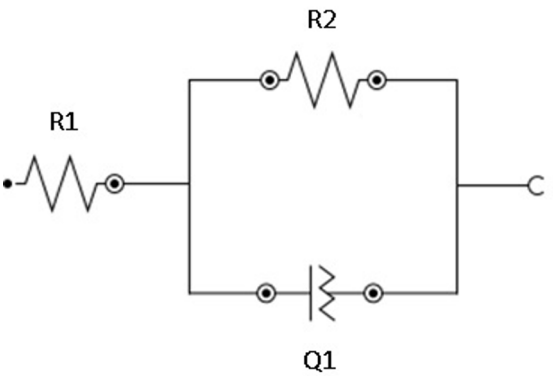

Figure 6. EEC used to simulate the experimental EIS data.

Table 2. EIS fitting parameters for the AISI 409 stainless steel after immersion for one hour in 0.1 M NaCl solution at room temperature.

$R_1(\Omega.cm^2)$	$Q_1(10^{-7}.F.cm^{-2}.s^{\alpha-1})$	n_1	$R_2(k\Omega.cm^2)$
13.1	6.79	0.94	665

The thickness of the passive film can be estimated using the EIS fitted data. The effective capacitance (C) can be calculated from the value of Q according to equations (2) and (3)[33]. In these equations, α is the CPE exponent, $Z_j(f)$ is the imaginary impedance value for a given frequency (f), Re is the electrolyte resistance, and Rt is the charge transfer resistance. The values of Re and Rt were obtained from Table 2 as given the by fitting the experimental EIS data with the EEC shown in Fig. 6. The value of α was graphically determined according to the procedure described by Orazem et al.[33] by plotting the modulus of the imaginary part of

impedance (|Zj|) versus the applied frequency (f) as shown in Fig. 7. This value was 0.95 and corresponds to the slope of the linear part of the |Zj| vs. f plot in the middle to low frequency range that is related to the response of the passive layer. The value of Q_{eff} was graphically determined from the linear part of the plot of Q versus the applied frequency f, as indicated in Fig. 8. The effective capacitance (C_{eff}) was, therefore, calculated using equation (3). Next, the thickness of the passive film (L) can be calculated from equation (4)[34] where ε_0 is the vacuum permittivity ($8.85.10^{-14}$ F.cm^{-1}) and ε is the dielectric constant of the passive film which can be assumed as 15.6 for stainless steels[35,36]. Using these values the thickness of the passive film was determined as 14.5 nm which is higher than other reported values for the passive film in stainless steels in low-chloride containing solutions (0.5 nm to 6 nm)[37-40]. The high charge transfer resistance (R_2) reported in Tab. 2 can be due to this relatively thick passive film.

$$Q = \sin\left(\frac{\alpha\pi}{2}\right)\frac{-1}{Z_j(f)(2\pi f)^{\alpha}} \quad (2)$$

$$C_{eff} = Q_{eff}^{1/\alpha}\left(\frac{R_e R_t}{R_e + R_t}\right)^{\frac{(1-\alpha)}{\alpha}} \quad (3)$$

$$L = \frac{\varepsilon.\varepsilon_0}{C_{eff}} \quad (4)$$

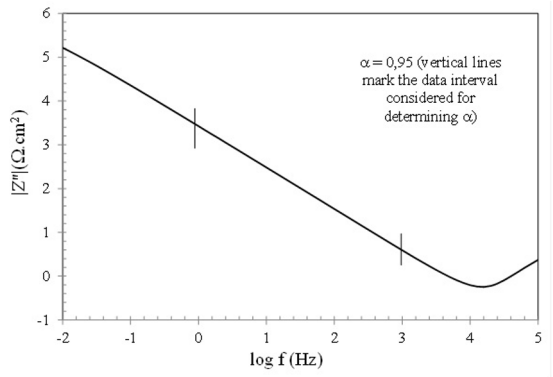

Figure 7. Determination of the α parameter, following the procedure described by Orazem et al.[31]

3.2.2 Mott-Schottky analysis

The passive film on the AISI 409 stainless steel was further characterized by investigating its semiconducting properties using the Mott-Schottky approach. The semiconducting behavior is due to the presence of intrinsic point defects in the passive film, leading to an extrinsic semiconductor behavior. Cation interstitials, cations vacancies and oxygen vacancies are the main defects of passive films on stainless steels. The Mott-Schottky approach is often used to study the semiconductor properties of the passive films on these

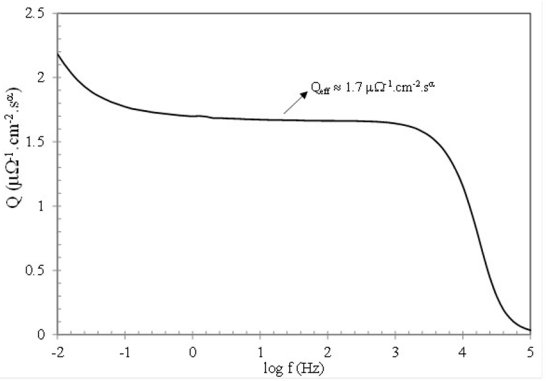

Figure 8. Determination of Q_{eff}, following the procedure described by Orazem et al.[31].

materials[41,42]. The n-type behavior is associated with electron donors and is related with the presence of oxygen vacancies and cation interstitials whereas the p-type behavior is associated with electron acceptors and is related to the presence of cation vacancies[43]. The Mott-Schottky relationships can be used to determine the type of semiconducting behavior and also the doping densities, according to equations (5) and (6) which are valid for n-type and p-type behaviors, respectively[44,45]. In these equations N_D and N_A are the donor and acceptor densities, e is the elementary charge, k is the Boltzmann constant, T is the absolute temperature, C is the capacitance, E is the applied potential, E_{FB} is the flat band potential, ε is the dielectric constant of the passive film (15.6 for stainless steels) and ε_0 is the vacuum permittivity ($8.85.10^{-14}$ F.cm^{-1}). The Mott-Schottky plot is obtained by plotting $1/C^2$ against E. A linear relationship with positive slope denotes the n-type behavior whereas a negative slope accounts for the p-type behavior[46,47].

$$\frac{1}{C^2} = \frac{2}{\varepsilon.\varepsilon_0.e.N_D}\left(E - E_{FB} - \frac{kT}{e}\right) \quad (5)$$

$$\frac{1}{C^2} = -\frac{2}{\varepsilon.\varepsilon_0.e.N_A}\left(E - E_{FB} - \frac{kT}{e}\right) \quad (6)$$

The Mott-Schottky plot of the AISI 409 stainless steel obtained after immersion for 24 h in 0.1 NaCl solution at room temperature is shown in Fig. 9.

Only one linear region was obtained throughout the applied potential range which displays a positive slope. This behavior is associated with n-type semiconducting character of the passive film, according to the Mott-Schottky theory. Considering the same potential range employed for the Mott-Schottky plots obtained in the present work, similar results have been reported for the passive films formed on stainless steels[48-50]. The positive slope indicates n-type semiconductor and is associated with the Fe-rich outer layer of the passive film formed on stainless steels where oxygen vacancies and cation interstitials are the major dopants[51]. The donor (N_D) density can be calculated from the linear part

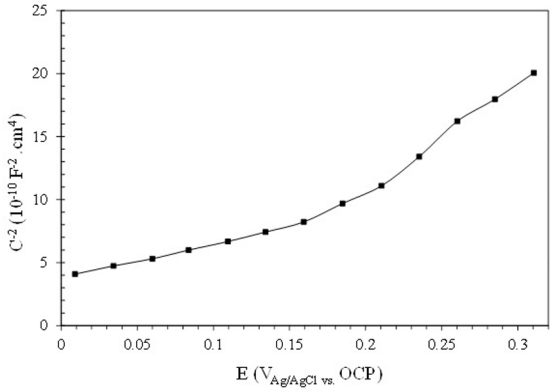

Figure 9. Mott-Schottky plot of the AISI 409 stainless steel after immersion for 24 h in 0.1 M NaCl solution at room temperature.

of the Mott-Schottky plot, according to equation (5). The value of N_D was determined as $2.25.10^{19}$ cm^{-3}. This value is of the same order of magnitude as other reported values for passive films formed on stainless steels[52] and indicate that oxygen vacancies and cation interstitials are the prominent dopants on the passive layer of the AISI 409 stainless steel.

The point defect model (PDM)[53,54] can be used to draw some conclusions about the passive film on the AISI 409 stainless steels. As stated in the PDM, oxygen vacancies on the surface of the passive film can react with chloride ions. In this respect, chloride ions are adsorbed into oxygen vacancies, generating cation/oxygen vacancy pairs. As a result, additional chloride ions can adsorb at the film/solution interface and, therefore, give rise to more cation vacancies. This process is autocatalytic. Passive film breakdown can occur as a result of excessive cation vacancies condensed during this process. In this respect, high donor densities in the passive film are associated with low resistance to pitting corrosion[55-57]. The results obtained in the present work point to a predominance of donors in the passive film formed on the AISI 409 stainless steel specimens that can lead to pitting susceptibility. The pitting corrosion behavior of the steel is characterized in the next sections.

3.2.3 Potentiostatic polarization

Current transients were monitored for 1800 s at +100 $mV_{Ag/AgCl}$ and +200 $mV_{Ag/AgCl}$ above the OCP after 24 h of immersion in 0.1 M NaCl solution at room temperature. The results are shown in Fig. 10. Current spikes in the potentiostatic polarization curve are indicative of pit nucleation and metastable pit growth[58]. A gradual increase of current density followed by sudden drop is typical of metastable events, indicating growth and repassivation of unstable pits[59]. This behavior was observed after 620 s for the sample tested at +100 mV (Fig. 10a). The maximum peak of current density was at approximately 0.0005 μA.cm^{-2} By increasing the applied potential to +200 mV the maximum current density related to the metastable events reached higher values (0.025 μA.cm^{-2}) (Fig. 10b).

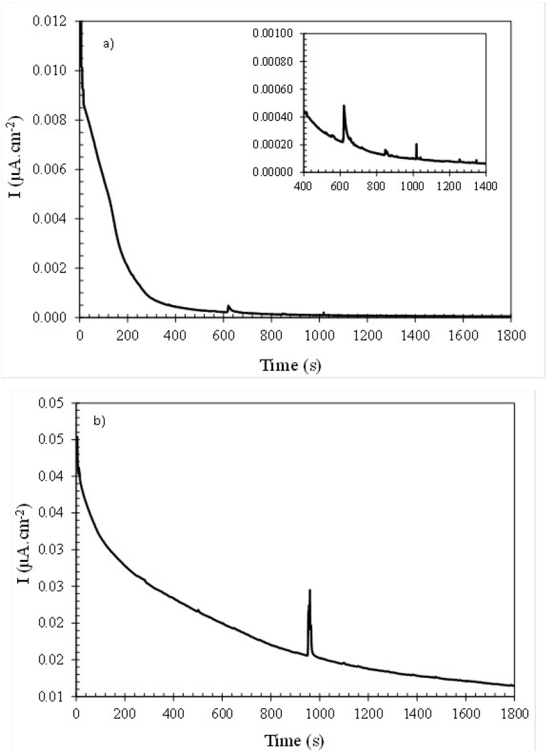

Figure 10. Current-time curves for the AISI 409 stainless steel immersed for 24 h in 0.1 M NaCl solution at room temperature at two anodic potentials: a) +100 $mV_{Ag/AgCl}$ vs. OCP; b) +200 $mV_{Ag/AgCl}$ vs. OCP).

A more quantitative approach was employed to study the metastable events. The radius of the metastable pits (r_{pit}) was estimated using Faraday's second law, according to equation (7). In this equation the pits are assumed to be hemispherical, M_w is the mean atomic weight of the alloy (56 g.mol^{-1}), n is the valence (2.16), F is Faraday's constant, ρ is the density of the alloy (7.8 g.cm^{-3}), I_{peak} is the current density at the peak, I_{bg} is the current density at the background and t is the time of the event. Following this methodology an average value of 41 nm was found for the metastable pits formed at +100 mV and 151 nm for those formed at +200 mV. These results show the susceptibility of the AISI 409 stainless steel to pitting corrosion and can be related to the n-type semiconducting behavior of the passive film as determined from the Mott-Schottky plot in Fig. 9.

$$r_{pit} = \left[\left(\frac{3M_w}{2\pi nF\rho}\right)\int_{t\,i}^{t\,f}(I_{peak} - I_{bg})dt\right]^{1/3} \qquad (7)$$

3.2.4 Potentiodynamic polarization

The pitting corrosion susceptibility of the AISI 409 stainless steel was further evaluated by potentiodynamic polarization. The test was carried out in 0.1 M NaCl solution at room temperature. The Tafel plot is shown in Fig. 11. The onset of stable pit growth is indicated by the breakdown potential (E_b), corresponding to the potential at which the current density presents a sharp increase, as indicated in

Fig. 11. In addition, the passive current density (I_{pass}) could be determined as well as the passive range ($\Delta E = E_b - E_{corr}$, where E_{corr} is the corrosion potential). The average values of these parameters are shown in Table 3. Following Ningshen et al.[60] the passive current density was determined at the middle of the passive range. These values are compatible with other reported values for ferritic and austenitic stainless steels in NaCl aqueous solutions[13,61]. Notwithstanding, this result confirm the susceptibility of the AISI 409 to pitting corrosion. Furthermore, the values of the parameters shown in Table 3 can be considered relatively low when compared to optimized stainless steel surfaces[62].

Table 3. Parameters obtained from the potentiodynamic polarization test.

E_b(V)	I_{pass}(μA.cm^{-2})	Passivity range (V)
0.59±0.05	1.91±1.04	0.61±0.12

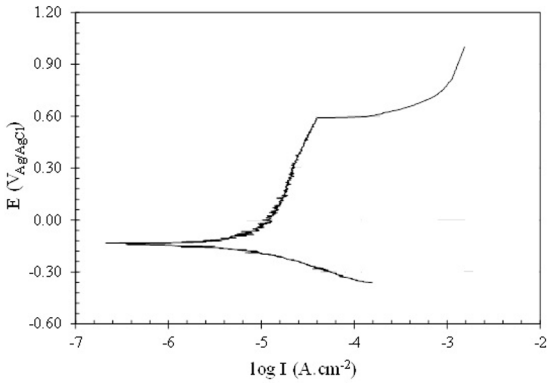

Figure 11. Tafel plot for the AISI 409 stainless steel after 24 h of immersion in 0.1 M NaCl solution at room temperature.

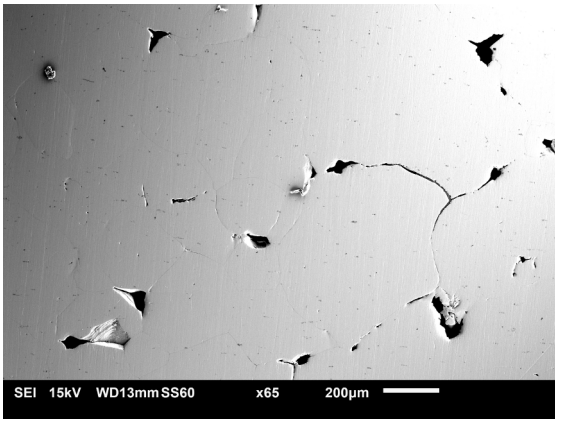

Figure 13. SEM micrograph of the AISI 409 stainless steel after potentiostatic polarization in 0.1 M NaCl solution at room temperature.

3.3 Pit nucleation sites

In order to identify preferential pit nucleation sites samples of the AISI 409 stainless steel were examined after the potentiodynamic polarization test using CLSM. Figure 12 shown two selected CLSM images of the AISI 409 stainless steel after potentiodynamic polarization in 0.1 M NaCl solution at room temperature. Figure 12a shows a region of dissolution around a gold-colored precipitate. This type of precipitate is reported to be TiN for Ti-stabilized ferritic stainless steels[7]. Figure 12b shows a small pit formed in the boundary of a grey-colored precipitate. These precipitates were identified by SEM/EDS analysis as described in section 3.1 and are mainly composed of titanium.

Further characterization of the pit site was carried out using SEM/EDS analysis. Figure 13 shows stables pits formed after

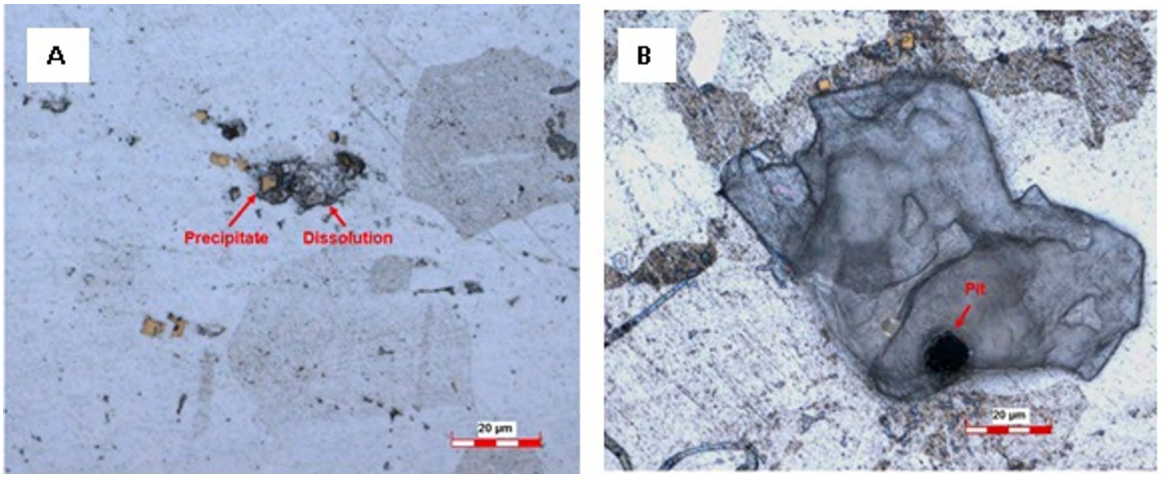

Figure 12. CLSM images of the AISI 409 stainless steel after potentiodynamic polarization in 0.1 M NaCl solution at room temperature: a) Dissolution around a gold-colored precipitate; b) pit formed in the boundary of a grey-colored precipitate.

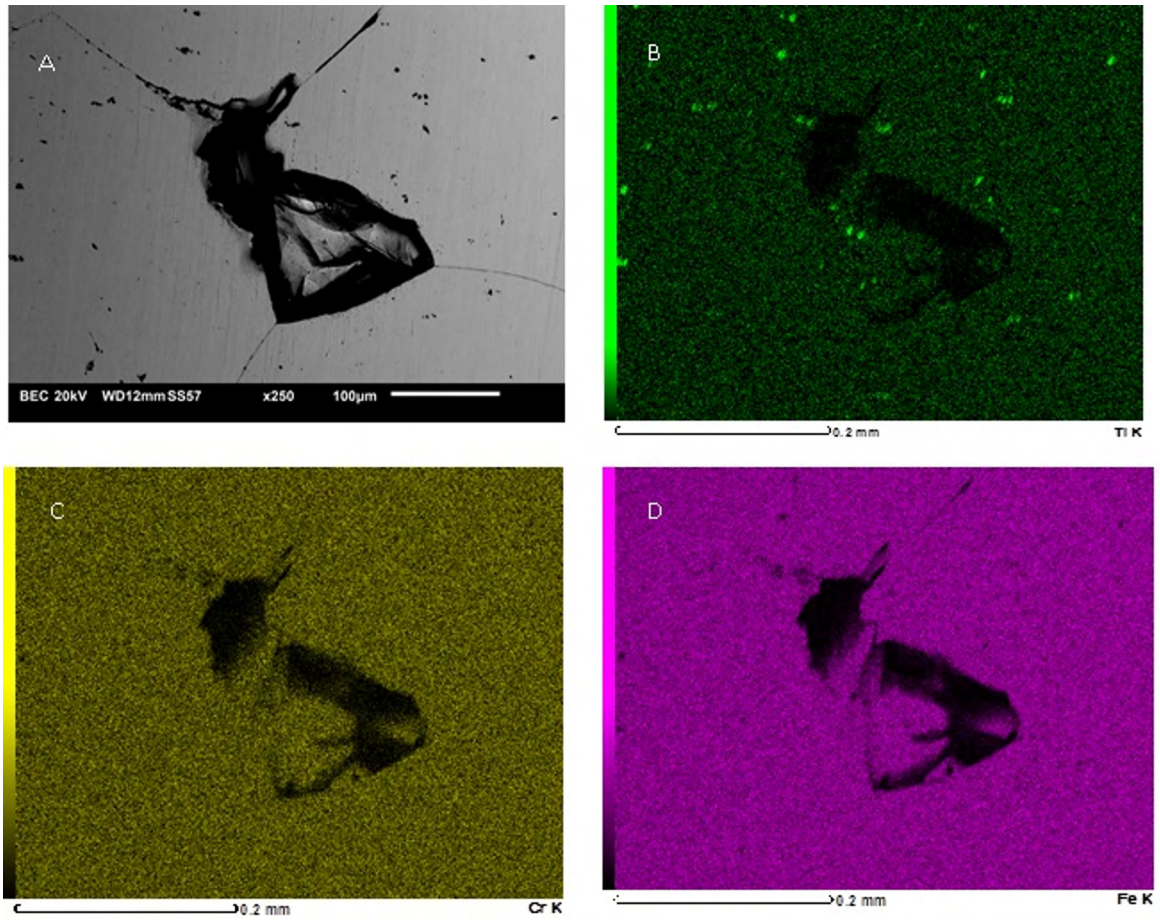

Figure 14. a) SEM micrograph of the AISI 409 stainless steel after potentiostatic polarization, showing a pit at grain boundaries intersections and dark small Ti-rich precipitates; EDS elemental mapping for: b) Ti; c) Cr and d) Fe.

potentiostatic polarization in 0.1 M NaCl solution at room temperature. Some grain boundaries are visible. Pit formed mainly at these sites. EDS elemental mapping of selected pits was performed in order to search for compositional features that could be related to the more active corrosion response of these sites. The area used for elemental mapping is shown in the SEM micrograph displayed in Fig. 14a. It shows several small dark regions spread through the observed area and one pit located at grain boundaries intersection between neighbor grains. EDS mapping for Ti, Cr and Fe are displayed in Figs. 14b, 14c and 14d, respectively. Cr and Fe signals arise from the AISI 409 matrix, being homogeneously distributed throughout the whole area, excpet within the pit cavity and in some small dark spots. The dark spots are Ti-rich areas as indicated in Fig. 14b. It is seen that pit formation occurred preferentially at grain boundaries intersections and is not necessarily associated with Ti-rich areas. Notwithstanding, Ti-rich areas are found inside the grains and also at the grain boundaries. In this respect, the high energy grain boundary sites were the preferential regions for the onset of pitting corrosion and this effect could be enhanced by precipitation of cathodic Ti-rich precipitates.

4. Conclusions

The pitting corrosion of AISI 409 stainless steel was studied. The microstructure of the alloy consists of a ferrite matrix and titanium-rich precipitates. The passive film on the surface of the alloy presents n-type semiconductive character that favors adsorption of chloride ions according to the point defect model. The susceptibility to pitting corrosion was confirmed by potentiostatic and potentiodynamic tests. Metastable pitting was studied at the anodic potentials of +100 mV and +200 mV above the open circuit potential. Metastable pit radius was estimated as 41 nm and 151 nm after the tests conducted at 100 mV and 200 mV vs OCP, respectively. Pit nucleation sites were mainly grain boundaries intersections. Ti-rich particles were eventually found at the pit nucleation sites. However, pitting corrosion was not detect around Ti-rich precipitates when they were located inside the ferrite grains.

5. Acknowledgements

Authors are thankful to the Brazilian agency CAPES for the financial support. Dr. Nelson Batista de Lima (IPEN/CNEN-SP) is kindly acknowledged for the XRD analysis.

6. References

1. Metal Suppliers Online. *Stainless Steel 409*. Available from: <http://www.suppliersonline.com/propertypages/409.asp>. Access in: 08/09/2017.
2. Burkert A, Lehmann J, Burkert A, Mietz J, Gümpel P. Technical and economical stainless steel alternatives for civil engineering applications. *Materials and Corrosion*. 2014;65(11):1080-1095.
3. Bitondo C, Bossio A, Monetta T, Curioni M, Bellucci F. The effect of annealing on the corrosion behavior of 444 stainless steel for drinking water applications. *Corrosion Science*. 2014;87:6-10.
4. ASM Handbook. *Corrosion: Fundamentals, Testing, and Protection. Vol. 13A*. Materials Park: ASM International; 2005.
5. Wang HP, Sun LF, Shi JJ, Liu CJ, Jiang MF, Zhang C. Inclusions and solidification structures of high pure ferritic stainless steels dual stabilized by niobium and titanium. *Rare Metals*. 2014;33(6):761-766.
6. Leban MB, Tisu R. The effect of TiN inclusions and deformation-induced martensite on the corrosion properties of AISI 321 stainless steel. *Engineering Failure Analysis*. 2013;33:430-438.
7. Michelic SK, Loder D, Reip T, Barani AA, Bernhard C. Characterization of TiN, TiC and Ti(C,N) in titanium-alloyed ferritic chromium steels focusing on the significance of different particle morphologies. *Materials Characterization*. 2015;100:61-67.
8. Kaewkumsai S, Auampan S, Wongpinkaew K, Viyanit E. Root cause analysis for 316L stainless steel tube leakages. *Engineering Failure Analysis*. 2014;37:53-63.
9. Sharma P, Roy H. Pitting corrosion failure of an AISI stainless steel pointer rod. *Engineering Failure Analysis*. 2014;44:400-407.
10. Nazir MH, Khan ZA, Saeed A, Stokes K. A predictive model for life assessment of automotive exhaust mufflers subject to internal corrosion failure due to exhaust gas condensation. *Engineering Failure Analysis*. 2016;63:43-60.
11. Balusamy T, Kumar S, Narayanan TSNS. Effect of surface nanocrystallization on the corrosion behaviour of AISI 409 stainless steel. *Corrosion Science*. 2010;52(11):3826-3834.
12. Ha YH, Park CJ, Kwon HS. Effects of non-metallic inclusions on the initiation of pitting corrosion in 11% Cr ferritic stainless steel examined by micro-droplet cell. *Corrosion Science*. 2007;49(3):1266-1275.
13. Van Niekerk CJ, Du Toit M. Sensitization behaviour of 11-12% Cr AISI 409 stainless steel during low heat input welding. *Journal of the South African Institute of Mining and Metallurgy*. 2011;111(4):243-256.
14. Kim JK, Kim YH, Lee JS, Kim KY. Effect of chromium content on intergranular corrosion and precipitation of Ti-stabilized ferritic stainless steels. *Corrosion Science*. 2010;52(5):1847-1852.
15. Kim JK, Kim YH, Uhm SH, Lee JS, Kim KY. Intergranular corrosion of Ti-stabilized 11 wt% Cr ferritic stainless steel for automotive exhaust systems. *Corrosion Science*. 2009;51(11):2716-2723.
16. Lloyd GF. Atomic number and crystallographic contrast images with the SEM: a review of backscattered electron techniques. *Mineralogical Magazine*. 1987;51:3-19.
17. Pandya S, Ramakrishna KS, Annamalai AR, Upadhyaya A. Effect of sintering temperature on the mechanical and electrochemical properties of austenitic stainless steel. *Materials Science and Engineering A*. 2012; 556: 271-277.
18. Lv J, Liang T, Dong L, Wang C. Influence of sensitization on microstructure and passive property of AISI 2205 duplex stainless steel. *Corrosion Science*. 2016;104:144-151.
19. Liu C, Bi Q, Leyland A, Matthews A. An electrochemical impedance spectroscopy study of the corrosion behaviour of PVD coated steels in 0.5 M NaCl aqueous solution: Part II.: EIS interpretation of corrosion behavior. *Corrosion Science*. 2003;45(6):1257-1273.
20. Zhang X, Fan L, Xu Y, Li J, Xiao X, Jiang L. Effect of aluminum on microstructure, mechanical properties and pitting corrosion resistance of ultra-pure 429 ferritic stainless steels. *Materials & Design (1980-2015)*. 2015;65:682-689.
21. Hu W, Xu J, Lu X, Hu D, Tao H, Munroe P, et al. Corrosion and wear behaviours of a reactive-sputter-deposited Ta_2O_5 nanoceramic coating. *Applied Surface Science*. 2016;368:177-190.
22. Xu A, Zhang F, Luo B, Jin F, Zhang T. Investigation the deterioration process of organic coating using changing rate of phase angle at high frequency united to neural network. *International Journal of Electrochemical Science*. 2013;8:773-779.
23. Bai Y, Deng Y, Zheng Y, Li Y, Zhang R, Lv Y, et al. Characterization, corrosion behavior, cellular response and *in vivo* bone tissue compatibility of titanium-niobium alloy with low Young's modulus. *Materials Science and Engineering: C*. 2016;59:565-576.
24. Galván JC, Larrea MT, Braceras I, Multigner M, González-Carrasco JL. *In vitro* corrosion behaviour of surgical 316LVM stainless steel modified by Si^+ ion implantation - An electrochemical impedance spectroscopy study. *Journal of Alloys and Compounds*. 2016;676:414-427.
25. Boissy C, Alemany-Dumont C, Normand B. EIS evaluation of steady-state characteristic of 316L steel passive film grown in acidic solution. *Electrochemistry Communications*. 2013;26:10-12.
26. Orazem ME, Tribollet B. *Electrochemical Impedance Spectroscopy*. Hoboken: John Wiley & Sons; 2011.
27. Fattah-alhosseini A, Vafaeian S. Comparison of electrochemical behavior between coarse-grained and fine-grained AISI 430 ferritic stainless steel by Mott-Schottky and EIS measurements. *Journal of Alloys and Compounds*. 2015;639:301-307.
28. Ben Salah M, Sabot R, Refait P, Liascukiene I, Méthivier C, Landoulsi J, et al. Passivation behavior of stainless steel (UNS N-08028) in industrial or simplified phosphoric acid solutions at different temperatures. *Corrosion Science*. 2015:99:320-332.
29. Lv J, Luo H. Comparison of corrosion behavior between coarse grained and nano/ultrafine grained 304 stainless steel by EWF,

XPS and EIS. *Journal of Nuclear Materials*. 2014;452(1-3):469-473.

30. Zhang LJ, Fan JJ, Zhang Z, Cao FH, Zhang JQ, Cao CN. Study on the anodic film formation process of AZ91D magnesium alloy. *Electrochimica Acta*. 2007;52(17):5325-5333.

31. Fattah-alhosseini A, Vafaeian S. Influence of grain refinement on the electrochemical behavior of AISI 430 ferritic stainless steel in an alkaline solution. *Applied Surface Science*. 2016;360(Pt B):921-928.

32. Bastos AC, Ferreira MG, Simões AM. Corrosion inhibition by chromate and phosphate extracts for iron substrates studied by EIS and SVET. *Corrosion Science*. 2006;48(6):1500-1512.

33. Orazem ME, Pébère N, Tribollet B. Enhanced graphical representation of electrochemical impedance data. *Journal of the Electrochemical Society*. 2006;153(4):B129-B136.

34. Fattah-alhosseini A, Saatchi A, Golozar MA, Raeissi K. The passivity of AISI 316L stainless steel in 0.05 M H_2SO_4. *Journal of Applied Electrochemistry*. 2010;40(2):457-461.

35. Orazem ME, Frateur I, Tribollet B, Vivier V, Marcelin S, Pébère N, et al. Dielectric properties of materials showing Constant-Phase-Element (CPE) impedance response. *Journal of the Electrochemical Society*. 2013;160(6):C215-C225.

36. Carmezim MJ, Simões AM, Montemor MF, da Cunha Belo MD. Capacitance behaviour of passive films on ferritic and austenitic stainless steel. *Corrosion Science*. 2005;47(3):581-591.

37. BenSalah M, Sabot R, Triki E, Dhouibi L, Refait P, Jeannin M. Passivity of Sanicro28 (UNS N-08028) stainless steel in polluted phosphoric acid at different temperatures studied by electrochemical impedance spectroscopy and Mott-Schottky analysis. *Corrosion Science*. 2014;86:61-70.

38. Niu W, Lillard RS, Li Z, Ernst F. Properties of The Passive Film Formed on Interstitially Hardened AISI 316L Stainless Steel. *Electrochimica Acta*. 2015;176:410-419.

39. Heuer AH, Kahn H, Ernst F, Michal GM, Hovis DB, Rayne RJ, et al. Enhanced corrosion resistance of interstitially hardened stainless steel: Implications of a critical passive layer thickness for breakdown. *Acta Materialia*. 2012;60(2):716-725.

40. Olsson COA, Landolt D. Passive films on stainless steels - chemistry, structure and growth. *Electrochimica Acta*. 2003;48(9):1093-1104.

41. Li DG, Wang JD, Chen DR, Liang P. Influences of pH value, temperature, chloride ions and sulfide ions on the corrosion behaviors of 316L stainless steel in the simulated cathodic environment of proton exchange membrane fuel cell. *Journal of the Power Sources*. 2014;272:448-456.

42. Feng X, Lu X, Zuo Y, Zhuang N, Chen D. The effect of deformation on metastable pitting of 304 stainless steel in chloride contaminated concrete pore solution. *Corrosion Science*. 2016;103:223-229.

43. Iken H, Basseguy R, Guenbour A, Ben-Bachir A. Classic and local analysis of corrosion behaviour of graphite and stainless steels in polluted phosphoric acid. *Electrochimica Acta*. 2007;52(7):2580-2587.

44. Hamadou L, Kadri A, Benbrahim N. Impedance investigation of thermally formed oxide films on AISI 304L stainless steel. *Corrosion Science*. 2010;52(3):859-864.

45. Fernández-Domene RM, Blasco-Tamarit E, García-García DM, García-García J. Effect of alloying elements on the electronic properties of thin passive films formed on carbon steel, ferritic and austenitic stainless steels in a highly concentrated LiBr solution. *Thin Solid Films*. 2014;558:252-258.

46. Gomes WP, Vanmaekelbergh D. Impedance spectroscopy at semiconductor electrodes: Review and recent developments. *Electrochimica Acta*. 1996;41(7-8):967-973.

47. Paredes EC, Bautista A, Alvarez SM, Velasco F. Influence of the forming process of corrugated stainless steels on their corrosion behaviour in simulated pore solutions. *Corrosion Science*. 2012;58:52-61.

48. Lv J, Liang T. Improved corrosion resistance of 316L stainless steel by nanocrystalline and electrochemical nitridation in artificial saliva solution. *Applied Surface Science*. 2015;359:158-165.

49. Yazici M, Çmakli O, Yetim T, Yetim AF, Çelik A. The effect of plasma nitriding temperature on the electrochemical and semiconducting properties of thin passive films formed on 316 L stainless steel implant material in SBF solution. *Surface and Coatings Technology*. 2015;261:181-188.

50. Lv J, Luo H. Comparison of corrosion properties of passive films formed on phase reversion induced nano/ultrafine-grained 321 stainless steel. *Applied Surface Science*. 2013;280:124-131.

51. Taveira LV, Montemor MF, da Cunha Belo M, Ferreira MG, Dick LFP. Influence of incorporated Mo and Nb on the Mott-Schottky behaviour of anodic films formed on AISI 304L. *Corrosion Science*. 2010;52(9):2813-2818.

52. Lv J, Liang T, Wang C, Guo T. Effect of in site strain on passivated property of the 316L stainless steels. *Materials Science and Engineering: C*. 2016;61:32-36.

53. Nicic I, Macdonald DD. The passivity of Type 316L stainless steel in borate buffer solution. *Journal of Nuclear Materials*. 2008;379(1-3):54-58.

54. Gui Y, Zheng ZJ, Gao Y. The bi-layer structure and the higher compactness of a passive film on nanocrystalline 304 stainless steel. *Thin Solid Films*. 2016;599:64-71.

55. Shahryari A, Omanovic S. Improvement of pitting corrosion resistance of a biomedical grade 316LVM stainless steel by electrochemical modification of the passive film semiconducting properties. *Electrochemistry Communications*. 2007;9(1):76-82.

56. Li WS, Luo JL. Uniformity of passive films formed on ferrite and martensite by different inorganic inhibitors. *Corrosion Science*. 2002;44(8):1695-1712.

57. Tang Y, Zhao X, Mao J, Zuo Y. The electrochemical characteristics of pitting for two steels in phosphate buffer solution with chloride. *Materials Chemistry and Physics*. 2009;116(2-3):484-488.

58. Tang Y, Zuo Y, Wang J, Niu B, Lin B. The metastable pitting potential and its relation to the pitting potential for four materials in chloride solutions. *Corrosion Science*. 2014;80:111-119.

59. Tian W, Du N, Li S, Chen S, Wu Q. Metastable pitting corrosion of 304 stainless steel in 3.5% NaCl solution. *Corrosion Science*. 2014;85:372-379.

60. Ningshen S, Sakairi M, Suzuki K, Ukai S. The corrosion resistance and passive film compositions of 12% Cr and 15% Cr oxide dispersion strengthened steels in nitric acid media. *Corrosion Science*. 2014;78:322-334.

61. Lee JB, Yoon SI. Effect of nitrogen alloying on the semiconducting properties of passive films and metastable pitting susceptibility of 316L and 316LN stainless steels. *Materials Chemistry and Physics*. 2010;122(1):194-199.

62. Borgioli F, Galvanetto E, Bacci T. Low temperature nitriding of AISI 300 and 200 series austenitic stainless steels. *Vacuum*. 2016;127:51-60.